Seismic performance of Unbonded Fiber-Reinforced Elastomeric Isolators (UFREI) made by recycled rubber. Influence of suboptimal crosslinking

A.B. Habieb[(1)], A. Formisano[(2)], G. Milani[(3)], G. Pianese[(3)], D. Torrini[(3)]

(1): Department of Civil Engineering, Institut Teknologi Sepuluh Nopember, Surabaya, Indonesia
(2): Department of Structures for Engineering and Architecture, University of Naples Federico II, Naples, Italy
(3): Department of Architecture, Built environment and Construction Engineering, Politecnico di Milano, Milano, Italy

Abstract

Seismic base isolation is considered effective to reduce the vulnerability of structures and it represents an optimal retrofitting solution in terms of reliability and effectiveness. Nowadays, one of the most promising devices is the Unbonded Fiber Reinforced Elastomeric Isolator (UFREI), which is considered a low cost device, thanks to its lightweight, easy installation and the total absence of steel. In this study, recycled rubber in the form of reactivated EPDM has been used to produce UFREIs, combined with glass fiber reinforcement, a technology that reduces further productions costs and allows a certain susteneability. To be ready for structural application, the rubber used for assembling the devices must be vulcanized correctly to create the polymer crosslinking properly. As a matter of fact, all rubber mechanical properties are strongly affected by curing temperature and curing time.
In the present study, the performance of an UFREI prototype proposed by the authors for the seismic isolation of low-rise masonry buildings in Indonesia has been investigated through a series of experimental tests and numerical analyses, taking into account the different levels of vulcanization degree for the pads and focusing in particular on the mechanical consequences linked to their under-vulcanization. In particular two prototypes are considered, one vulcanized correctly at 150°C for 40 minutes and the other vulcanized in a standardized industrial process at 130°C for 40 minutes. The experimental characterization allows to calibrate the elastic and viscoelastic properties of the pads, to be used in advanced numerical simulations carried out in Abaqus to establish the cyclic behavior of the devices. A further identification procedure is proposed, substituting at structural level the device discretized with 3D elements with an equivalent mechanical system constituted by a non-linear spring and a dashpot. Numerical non-linear dynamic analyses carried out on a single storey masonry building subjected to a strong seismic event show that the devices vulcanized at 130°C for 40 minutes, although having suboptimal crosslinking and hence poor mechanical properties, are still suitable to effectively isolate low-rise buildings in developing countries. Moreover, being the under vulcanized device less rigid, it reduces more the seismic demand on the structure. Thus, low values of tensile damage have been registered.

Keywords: seismic isolation; fiber-reinforced elastomeric isolator (FREI); regenerated EPDM; vulcanization; masonry; non-linear dynamic analysis.

1. Introduction

Devastating earthquakes caused a lot of damages to structures and infrastructures in the recent past. Most of the high-seismic zones are located in developing countries (e.g. India, Indonesia, South and central America), where unreinforced masonry or poorly constrained masonry is generally employed in low-quality housing due to its relatively cheap cost. As a matter of fact, masonry is not so suitable in seismic areas being characterized by insufficient tensile strength, resulting in a low horizontal load carrying capacity. When an earthquake occurs, low-class buildings in developing countries experience many casualties.

To reduce the damaging effect on buildings due to earthquakes, the following techniques are commonly used: increase the seismic-resistant capacity of the structure [1][2], involve bracing systems [3][4], use added damping systems [5], reduce the seismic demand on the structure by incorporating base isolation systems [6][7][8]. Base seismic isolation is an effective strategy to reduce the vulnerability of new and existing structures and it represents an optimal retrofitting solution in terms of reliability and effectiveness. The isolation devices, which are typically placed at the base of the structures, shift the fundamental frequency of the structure to the range of the spectrum where spectral accelerations are lower.

During a seismic event, the base isolated structure is supposed to exhibit negligible inelastic deformation because the signal is filtered at the base level. Conventionally, steel-reinforced elastomeric (SREI) and friction based devices are used for base isolation of structures and actually, they represent the most used method of seismic isolation. These isolators are generally expensive due to the need of introducing thick steel plates for their supports. Thus, they are not so suitable for ordinary residential buildings, especially in developing countries.

Many alternatives have been studied in recent years to find a low-cost isolation device. Nowadays, one of the most promising is the Fiber Reinforced Elastomeric Isolator (FREI). In [9][10] fiberglass layers have been employed for the production of FREIs. They can be applied to the structures in several ways: bonded[11][12], unbonded [13], partially bonded [14] and with friction, in which there is no bonding between rubber pads and fiber layers.

Compared to SREIs, FREIs could be installed between the upper structure and the foundation without any bonding or fastening in the so called unbonded application, reducing hugely costs. Many experimental works have been published on UFREIs, revealing their advantages. First of all, the effective horizontal stiffness of UFREIs is considerably lower when compared with bonded ones, decreasing the seismic force demands [10][13][15]. This feature is a consequence of the so called rollover effect, a sort of quasi-rigid rotation occurring at large deformation under strong earthquakes.

Another important feature of UFREIs is the hardening which occurs at large deformation. This characteristic is due to the contact between isolator vertical edges and supports, which occurs at large deformations. It plays an important role in limiting the shear displacement during a severe seismic event [16][17][19].

Since the UFREIs are characterized by large deformability, many studies have investigated the stability limit at which the devices reach a state of damage or delamination. Some researchers have stated that this critical value is reached when a lateral displacement of 1.7-2 h_r (total height of the rubber pads) occurs [18]. Other authors [19] report that even larger displacements, equal to 3 h_r, do not cause any damage in the rubber-fiber interfaces. This high critical value allows to employ small-height isolators. To be ready for structural application, the rubber used for assembling the devices must be cured correctly to properly create the polymer network and make the rubber capable of sustaining vertical loads at the same time filtering the horizontal exitation. All rubber mechanical properties are strongly affected by curing temperature and curing time.

This paper is aimed at studying the effect of an undervulcanization on the mechanical properties of a real UFREI prototype, conceived for the application of low cost isolation in new masonry buldings in developing countries. The undervulcanization is a typical production error that suppliers do on purpose because of the impossibility to reach higher temperatures in standard electric ovens used in large scale productions. It is therefore quite common to deal with large stocks of low cost isolators where rubber pads have been treated at a temperature which is largely suboptimal.

This study is devoted to the structural analysis of an under vulcanized FREI cured at 130°C for 40 minutes, which is compared to the structural performance exhibited by a well-vulcanized one cured at 150°C for 40 minutes. The device is a real prototype produced by the authors within a research project aimed at applying UFREIs at low cost in new residential masonry buldings in Indonesia. The matter of the under-vulcanization has been studied to evaluate the possibility of employing such device taking into account the most meaningful errors in the production process, such as FRP-rubber bond defects, geometric irregularities in the FRP shims (a research still ongoing) caused by the insufficient flexural stiffness and inhomogeneous and suboptimal vulcanization of the pads.

The present paper focuses on this latter important aspect; in particular the performance of an UFREI prototype proposed by the authors for the seismic isolation of low-rise masonry buildings in Indonesia has been investigated through a series of experimental tests and numerical analyses, taking into account the different levels of vulcanization degree for the pads and focusing in particular on the mechanical consequences linked to their under-vulcanization. Two geometrically indentical prototypes are considered, one vulcanized correctly at 150°C for 40 minutes and the other vulcanized in a

standardized industrial process at 130°C for 40 minutes. The experimental characterization, obtained by means of stress-strain tests, hardness tests along the entire volume of the isolator and relaxation tests, allows to calibrate the elastic and viscoelastic properties of the pads, to be used in advanced FE numerical simulations conducted to establish the cyclic behavior of the devices. The numerical analyses are carried out in Abaqus with an heterogeneous discretization of the device, where rubber pads are modeled with 3D brick elements exhibiting a viscoelastic behavior (Yeoh elastic model coupled with a Maxwell viscosity model), FRP is assumed linear elastic and the unbonded condition in the upper and lower edges is simulated with contact interfaces. Cyclic numerical shear tests show that the under-vulcanization tends to reduce the shear stiffness of the single device, whereas the damping remains relatively stable. A further identification procedure is proposed, substituting at structural level the device discretized with 3D elements with an equivalent mechanical system constituted by a non-linear spring and a dashpot. Such identification allows to have a numerical insight into the effectiveness of the isolation applied on a realistic case study, where the masonry superstructure is modeled with a standard Concrete Damage Plasticity material. Usually, to study the masonry in a non-linear range, more complex models of the CDP should be used that take into account the orthotropic behavior [20][21]. However, for irregular textures, the behavior tends to be more similar to an isotropic one and the utilization of damaging/inelastic models available in commercial codes for concrete is admitted [22][23][24]. The validation of the identified spring-dashpot model is obtained simulating the behavior of an isolated heavy rigid RC slab excited with a real accelerogram. Two models are compared, the first obtained discretizing the four isolators placed at the slab corners with 3D FEs, the second substituting the devices with the coupled spring and dashpot system, whose mechanical properties are obtained from the identification carried out for the cyclic shear tests. The output in terms of accelerations registered on the RC slab confirm the effectiveness of the identification approach proposed. Finally, numerical non-linear dynamic analyses are carried out on a small single storey masonry building subjected to a strong seismic excitation. Simulations show that the devices vulcanized at 130°C for 40 minutes, although having suboptimal crosslinking and hence poor mechanical properties, are still suitable to effectively isolate low-rise buildings in developing countries. Moreover, being the under vulcanized device less rigid, it reduces more the seismic demand on the structure. Indeed, slightly lower values of tensile damage on the superstructure are observed.

2. UFREI 75 base seismic isolator

The device object of the study is constituted by five rubber pads (10 mm thick) of reactivated EPDM made with 2/3 of regenerated rubber and 1/3 of virgin rubber (Dutral 4038), and four GFRP laminas

(0.5 mm thick) with a square section of 75x75 mm (LxL) and a height equal to 65 mm (h_b) (Figure 1). The detailed composition of the rubber compound is presented in Table 1.

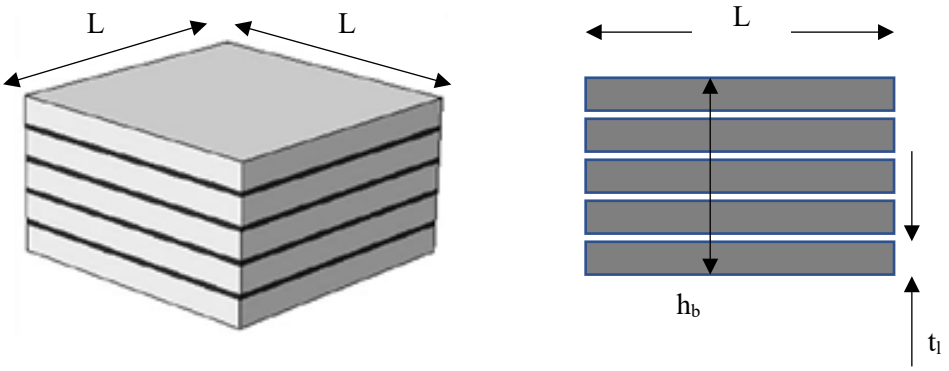

Figure 1: Design of the seismic base isolator UFREI 75

The results obtained in [25] show that the device cured with a temperature of 130°C for 40 minutes exhibits a non-uniform curing level. So, rubber mechanical properties are non-homogenous within the isolator. On the other hand, the curing temperature of 150°C leads to homogenous curing, with a homogeneous distribution of mechanical properties.

Table 1: Composition of rubber compound

Rubber Batch	
Ingredient	**gr**
EPDM Dutral 4038	100
EPDM regenerated B	300
ZnO	4
Stearina	1
Carbonato	40
N550 FEF II	185
Olio paraffinico	95
MBT PREMIX	1.5
ZOLFO PREMIX	2.5
TMTD PREMIX	2
TOTAL	**731**

To investigate the distribution of curing level for the under-vulcanized device, knife cuts on the middle vertical and diagonal sections have been done, and the Shore A Hardness has been measured with a digital Shore A durometer. As expected, the hardness varies from inner to outer points, passing from 48±2 Shore A to 60±2 Shore A, as visible in the color map in Figure 2. An identical trend is also observed along the device diagonal.

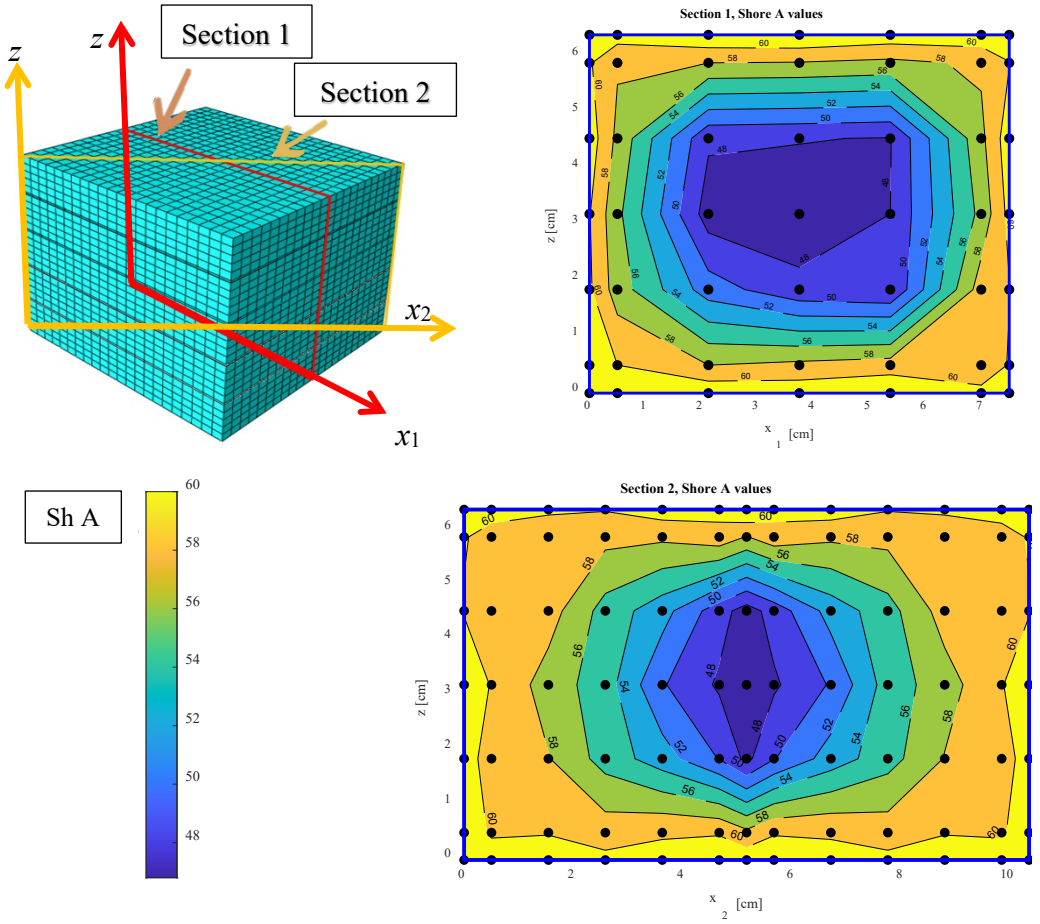

Figure 2: Shore A hardness measured on the middle vertical section and along the diagonal of a device cured at T=130° for 40 minutes

3. Rubber mechanical properties

Considering that the vulcanization at 130°C leads to a non homogeneus vulcanization, to characterize the rubber properties, stress-strain and relaxation tests were performed on rubber specimens vulcanized at 170°C, but assuming an insufficient exposition time, so to reduce the final hardness.

In particular, to obtain a suboptimal curing level in dumb bell laboratory samples used for the tests, taking into account that an optimal vulcanization is obtained by curing the specimens at 170°C for 10 minutes (which leads to a rubber compound with an expected hardness of 60 Shore A according to [26]), two families of rubber specimens were vulcanized at 170°C for 2 minutes and 2.5 minutes, respectively. In the following, the first is labeled as S -"Soft" and the latter as H -"Hard". Subsequently, Shore A hardness was measured on rubber samples with a thickness of 6 mm (obtained overlapping 3 pads 2 mm thick) according to ISO 7619-1 prescription [27]. Values of 50 Shore A and 53 Shore A were obtained respectively for the samples cured for 2 minutes and for those cured for 2.5 minutes, confirming that the vulcanization conditions used lead to an under vulcanization of the specimens.

3.1. Uniaxial tensile test on specimens S and H

For both S (i.e. soft, 50 Shore A rubber) and H (i.e. hard, 53 Shore A rubber) specimens, three fresh samples in the form of dumb bell pieces with an average thickness of 2 mm, see Figure 3a, have been tested in a uniaxial tensile test device (Figure 3b) based on ISO 37 [28]. The specimens have been stretched up to failure to define tensile strength and strain at failure (Figure 3c). The final stress-strain curves used to characterize the rubber behavior represent an average of three identical tests. In Figure 4, the experimental stress-strain curves are presented. As visible, both the specimens exhibit identical shapes of the curves. Even though the final strain and final stress values are comparable, as expected, the H specimens with a higher value of hardness are slightly stiffer.

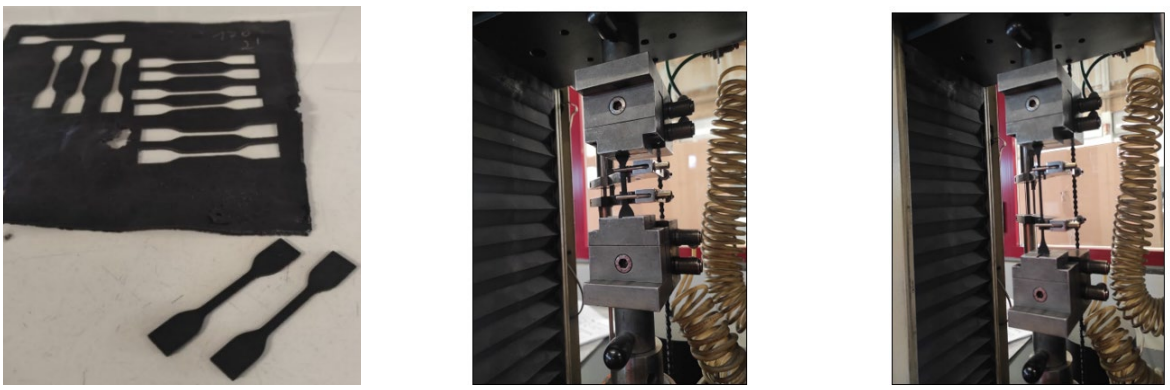

a) b) c)

Figure 3: Dumb-bell specimens of rubber (a), the uniaxial tensile test device (b), stretching of the rubber specimen (c)

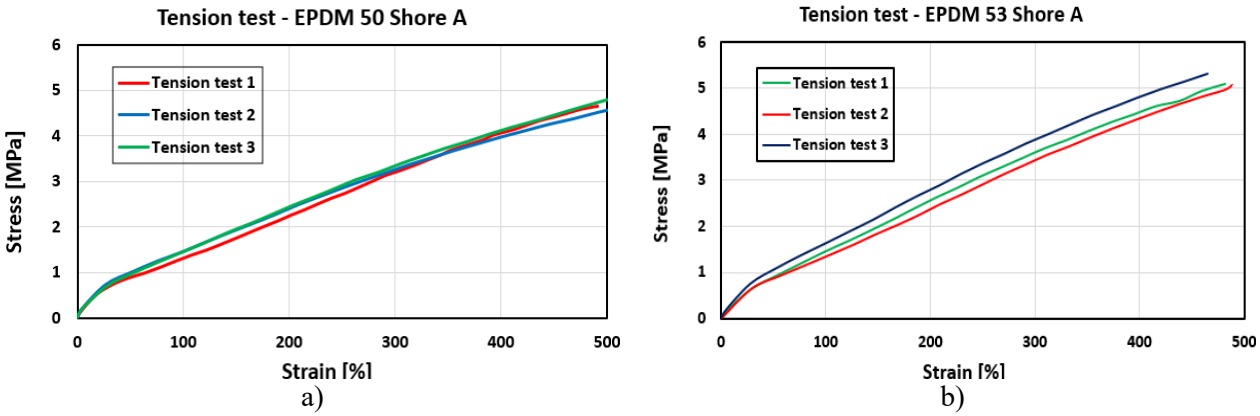

a) b)

Figure 4: Stress-strain curves for the S specimen (a) and H specimen (b)

Once the experimental stress-strain curves have been obtained, the data have been inserted into Abaqus [29] for material coefficients fitting. The rubber behavior could be modeled using hyperelastic models based on the strain energy density function and built in the software (Abaqus). For the present rubber compounds, the Yeoh model has been used [30], as expressed by Equation (1)

$$W = \sum_{i=1}^{3} C_{i0}(I_1 - 3)^i + \sum_{i=1}^{3} \frac{1}{D_1}(J_{el} - 3)^{2i} \quad (1)$$

In Figure 5, the experimental stress-strain curves are compared with the Yeoh model, that is perfectly capable to numerically represents the rubber hyperelasticity [31].

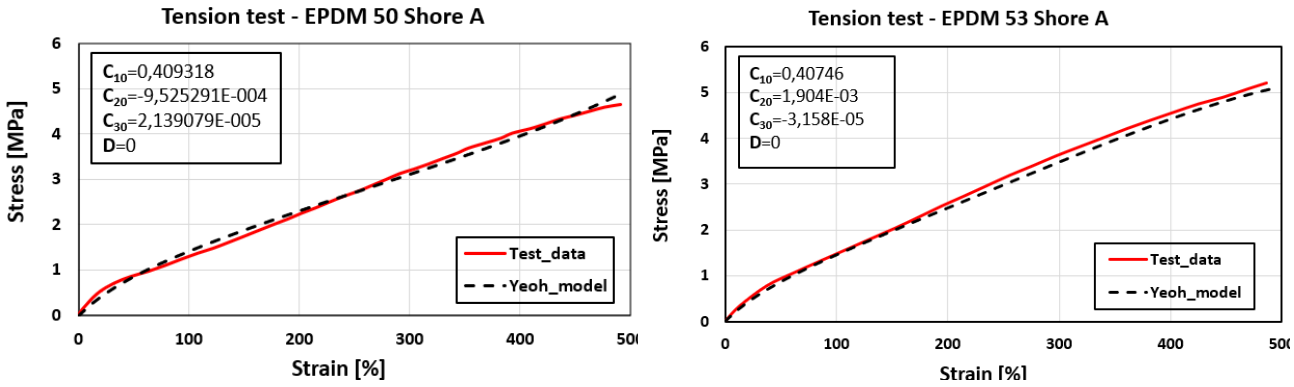

a) b)

Figure 5: Comparison between experimental data and Yeoh model for the specimens S (a) and H (b)

3.2.Relaxation test on specimens S and H

The viscoelasticity parameters of rubber material can be obtained from a relaxation test. During this test, the rubber specimen is subjected to a sudden strain, set at 150%, which is kept constant over time. After the first elastic phase, the rubber relaxes due to viscous effects. The device and the specimens used for the relaxation tests are the same used for the uniaxial tensile tests.

The tests have been performed on three identical samples for both S and H specimens. The final curve represents the average of the three results. Once the experimental data of the relaxation test have been obtained, the data have been transformed into normalized stress. In such curves, the initial stress at t=0s is the maximum value of the stress registered, normalized to 1. The relaxation has been conducted for 100 seconds because no remarkable stress reduction is observed after that period. Figure 6 and Figure 7 show the relaxation test curves and normalized stress curves for both compounds.

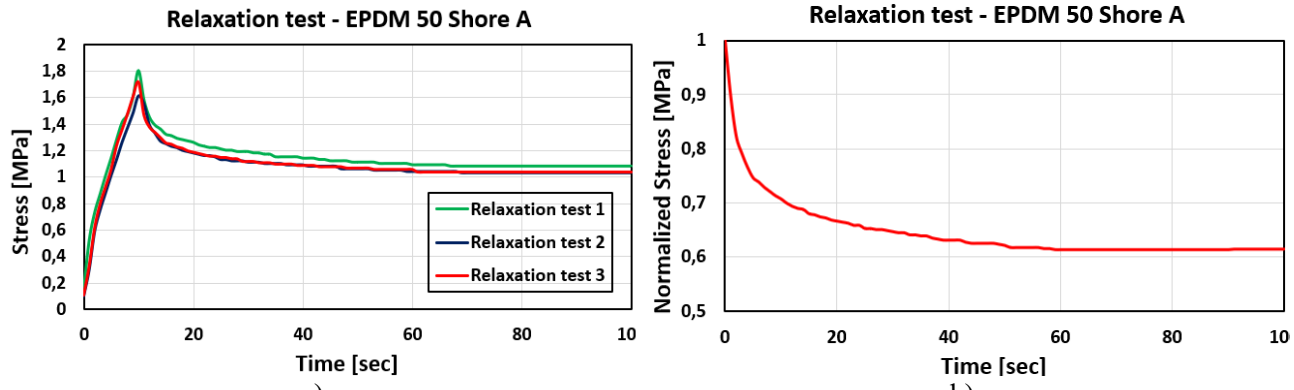

a) b)

Figure 6: Relaxation test curves (a) on three samples of rubber compound S with 50 Shore A hardness and

the normalized curve (b)

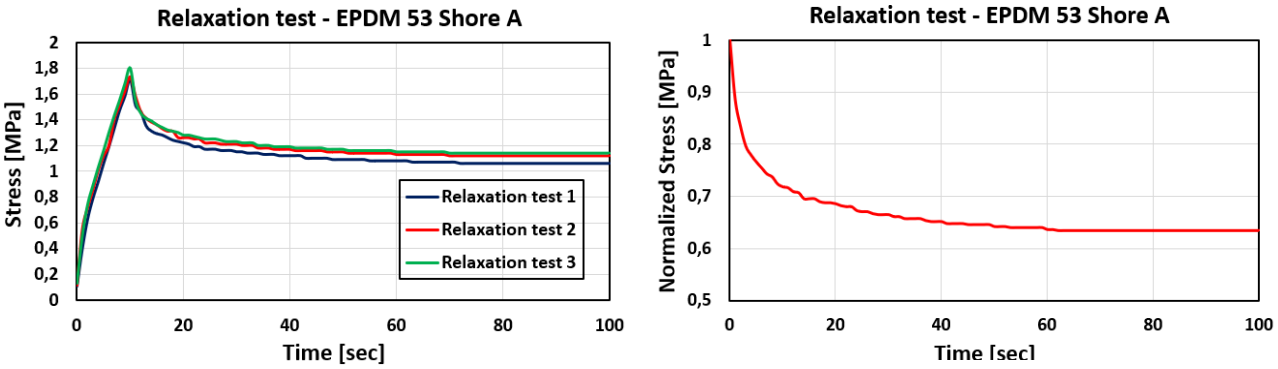

a) b)

Figure 7: Relaxation test curves (a) on three samples of rubber compound H with 53 Shore A hardness and the normalized curve (b)

The normalized relaxation curves can be fitted by Prony [32][33] series which is based on the viscoelastic generalized Maxwell model. It is a viscoelasticity model available in Abaqus to model the time-dependent stress-strain relationship as expressed in Equation (2).

$$G(t) = G_\infty + \sum_{k=1}^{K} G_k e^{-\frac{t}{\tau_k}} = G_0 \left[1 - \sum_{k=1}^{K} g_k (1 - e^{-\frac{t}{\tau_k}}\right] \quad (2)$$

The rheological model of the stress relaxation function G(t) is shown in Figure 8. As visible, the model is constituted by non-linear elastic springs representing the elastic response of rubber and a finite number of Maxwell elements (spring and dashpots) which describes viscoelastic behavior [34]. In Abaqus, the right side of Equation (2) is given in input, where the parameters have the following meaning:

- $G_0 = shear\ modulus\ at\ time\ t = 0\ s$;
- $g_k = dimensionless\ Prony\ coefficient$;
- $t_k = relaxation\ time\ defined\ as\ \frac{\eta_k}{G_k}$.

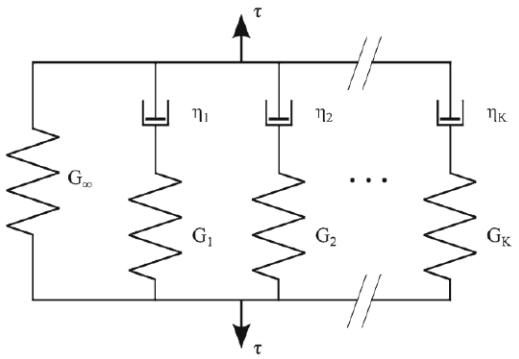

Figure 8: Rheological model of the relaxation function G(t)[34]

Figure 9 shows the comparison between the normalized experimental relaxation test curve and the Prony model in Abaqus. As visible, two Maxwell elements are sufficient to describe the rubber

viscoelasticity adequately.

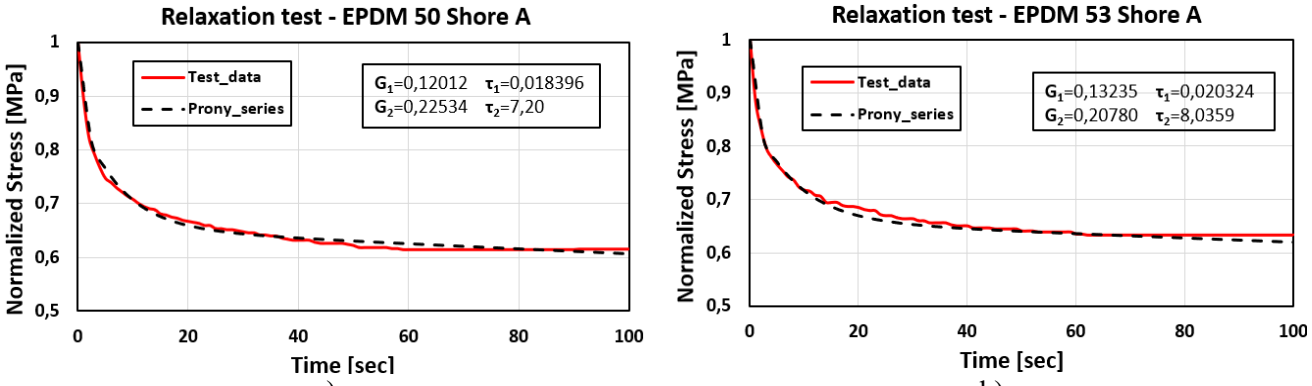

a) b)

Figure 9: Comparison between experimental test data and Prony viscoelastic model for the specimens S (a) and H (b)

4. Modeling of unbonded fiber reinforced elastomeric isolators

Once obtained the hyperelastic and viscoelastic properties of the rubber compounds, a detailed 3D FE analyses have been performed on a single UFREI. In particular, the device has been subjected to a 0.5 Hz cyclic horizontal displacement up to 50 mm (Total rubber height) applied at the top support, under constant vertical pressure of 2 MPa.

Two devices have been analyzed. The first one cured at 150°C for 40 minutes, with the rubber mechanical properties uniformly distributed, and the second cured at 130°C for 40 minutes, with a non-homogeneous distribution of rubber mechanical properties, which vary almost linearly within the isolator in accordance with the results shown in Section 2. Subsequentially, a spring-damper simplified model has been implemented in Abaqus instead of the detailed 3D isolator model to reduce the computational cost for the structural applications (Section 5).

4.1.3D FE modeling

The isolator has been modeled using almost 18000 eight-node brick (C3D8RH) elements with dimensions 3.5 x 3.5 x 2 mm. The final mesh is shown in Figure 10. In this study, an unbonded condition has been simulated. There is no bonding between the supports and the rubber pad. For this purpose, a penalty surface-interaction model has been introduced between the two surfaces, and a friction coefficient of μ=1 has been applied. On the contrary, a perfect bond using the surface-to-

surface tie constraint between rubber and GFRP has been adopted.

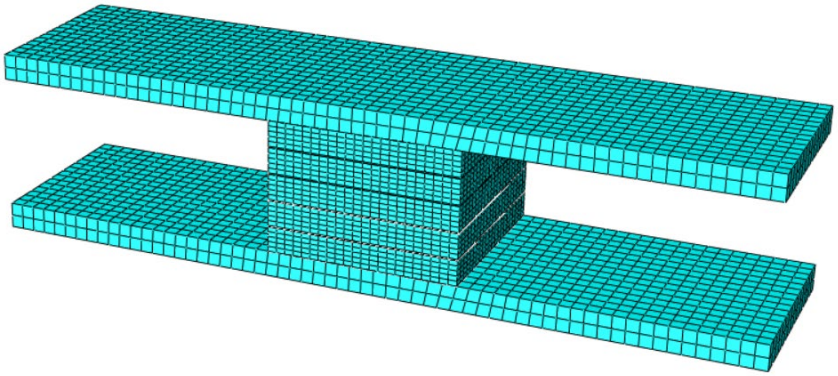

Figure 10: FE model of UFREI 75

Yeoh and Prony models have been used to represent the rubber behavior as described in section 3.1 and 3.2. Table 2 and Table 3 summarize the coefficients adopted for the Yeoh model and the Prony series. It is important to underline that the 60 Shore A rubber coefficients for Yeoh and Prony have been obtained in previous research [26]. The fiber has been assumed isotropic-elastic with a Young modulus of E=40000 MPa and a Poisson ratio υ=0.2, in accordance with many references [35][36][37].

Table 2: Yeoh model coefficient

Hardness [Shore A]	**C10**	**C20**	**C30**	**D**
50	0.40932	$-9.5252 \cdot 10^{-4}$	$2.13907 \cdot 10^{-5}$	0
53	0.40746	$1.9039 \cdot 10^{-3}$	$-3.1585 \cdot 10^{-5}$	0
60	0.722	0.019	$-8.5 \cdot 10^{-4}$	0

Table 3: Prony series coefficient

Hardness [Shore A]	**g1**	**τ_1**	**g2**	**τ_2**
50	0.120	0.018	0.225	7.20
53	0.132	$2.03 \cdot 10^{-2}$	0.207	8.03
60	0.254	0.103	0.145	3

To assign different mechanical properties to the model, the EPDM pad has been partitioned into several cubes, as visible in Figure 11. Then, three different pads have been considered: middle pad, intermediate pad, and external pad. On each pad, a different distribution of mechanical properties has been assigned, as visible in Figure 12 and Figure 13, where the red part is linked to 50 Shore A rubber properties, the orange one to 54 Shore A, and the green one to 60 Shore A. In Figure 14 are reported the final lateral force-displacement curves.

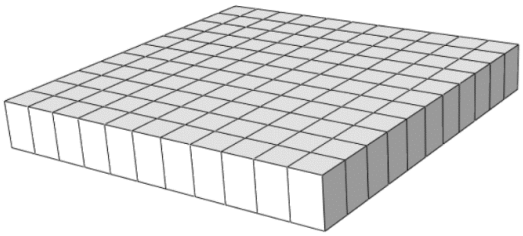

Figure 11: EPDM pad subdivided into several bricks in Abaqus

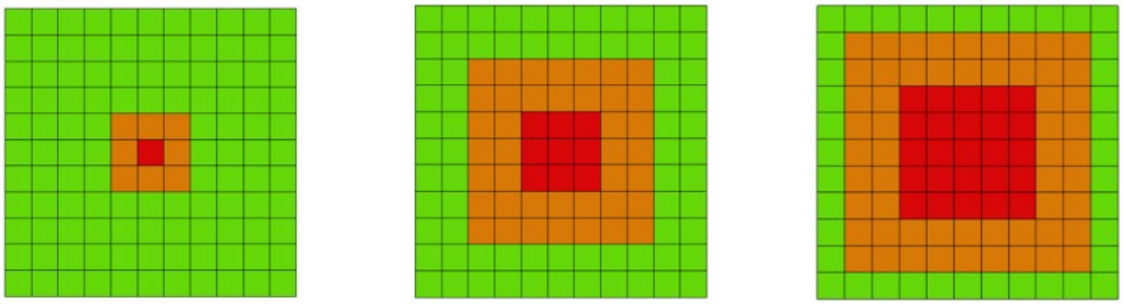

a) b) c)

Figure 12: Distribution of mechanical properties on external pad section (a), intermediate pad section (b), middle pad section (c)

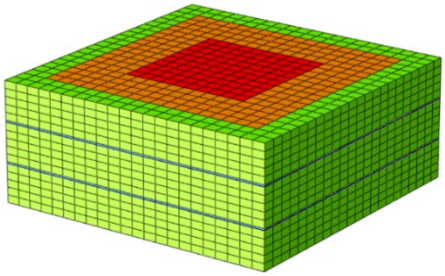

Figure 13: Middle horizontal section of UFREI cured at T=130°C

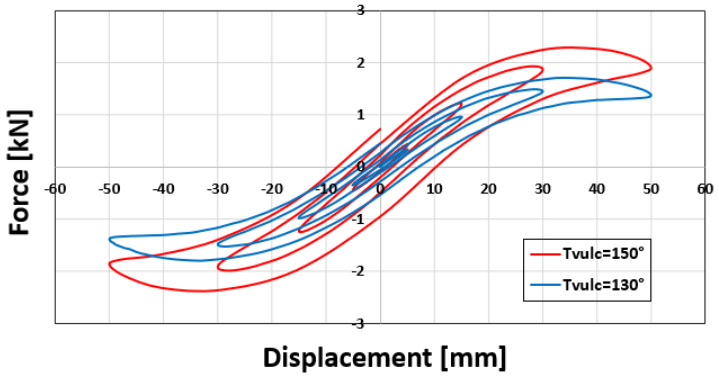

Figure 14: Comparison between lateral force-displacement curves for devices cured at 130°C and cured at 150°C

To compare the device structural response, effective horizontal stiffness $K_{H_{eff}}$ and damping ratio ξ

have been evaluated at four cycles with the maximum displacement equal to 5mm, 15mm, 30mm and 50mm, respectively. The computations are based on Equations (1)-(4). In Figure 15, a schematic representation of the main parameters used for the computations of the effective horizontal stiffness and damping ratio is presented, where W_d is the loop area. In Table 4 and in Table 5, the damping ratio and effective horizontal stiffness for each cycle are summarized.

$$K_{H,eff} = (F_{max} - F_{min})/(\Delta_{max} - \Delta_{min}) \quad (1)$$

$$\xi = W_d/(4\Pi W_s) \quad (2)$$

$$Ws = (1/2) * K_{H,eff} * \Delta^2_{max,ave} \quad (3)$$

$$\Delta_{max,ave} = (\Delta_{max} + \Delta_{min})/2 \quad (4)$$

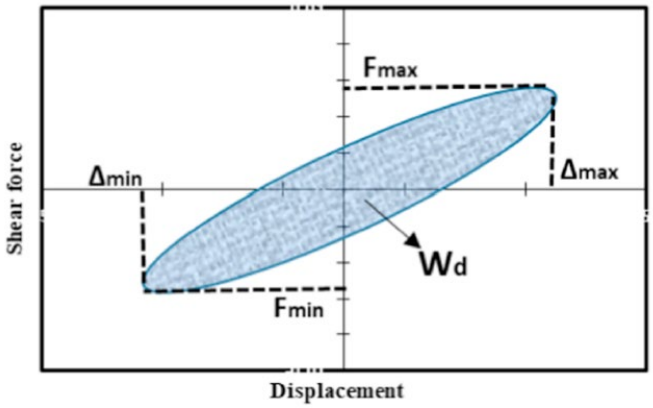

Figure 15: Main parameters used for the computation of effective horizontal stiffness and damping ratio

Moreover, to calibrate the simplified spring-damper model, the damping coefficient C has been evaluated using Equation (9):

$$C = \frac{F_0}{v} \quad (9)$$

in which:
$C = damping\ coefficient\ [\frac{N\ s}{mm}]$;
$v = velocity\ \left[\frac{mm}{s}\right]$;
$F_0 = Force\ at\ the\ end\ of\ each\ cycle\ [N]$.

Table 4: Damping ratio and Effective horizontal stiffness for each cycle on the device cured at 150° for 40 minutes

Cycle	Effective horizontal stiffness $K_{H,eff}$ [N mm]	Damping ratio ξ [%]
1°	87.65	7.86

2°	82.41	7.68
3°	65.34	10.01
4°	46.20	13.92

In both cases, the effective horizontal stiffness decreases passing from the first to the last cycle. This is a typical feature of unbonded application. In particular, the device experiences a rollover, which causes a non-linear behavior, decreasing the effective stiffness. Another remarkable feature in both the devices is the variation of damping ratio with the increase of lateral displacement.

Table 5: Damping ratio and Effective horizontal stiffness for each cycle on the device cured at 130° for 40 minutes

Cycle	Effective horizontal stiffness $K_{H,eff}$ [N mm]	Damping ratio ξ [%]
1°	67.59	6.38
2°	64.86	5.67
3°	50.30	7.73
4°	35.08	11.20

The comparison of the results summarized in Table 4 and in Table 5 shows that the device cured at 130°C is characterized by lower effective horizontal stiffness with respect to the one cured at 150°C. The same holds for the damping ratio.

4.2.Spring-damper simplified model

For large-scale seismic analysis of isolated structures, the use of detailed 3D FE models of isolators is very time-consuming. Therefore, in this study a simplified spring-damper model is used to represents the 3D isolator model. A single 3D isolator has been replaced using a paired axial connector in two orthogonal directions, introducing a non-linear spring and a constant damping coefficient.

Direct shear analysis on the 3D FE model using only instantaneous material mechanical properties has been performed. This allows to obtain a force-displacement curve without hysteretic behavior. Unlike the previous case, where the isolator experiences displacement up to 100% shear deformation, the analysis has been performed until the isolator experiences a hardening phase due to contact between its vertical edges and supports. In Figure 16, the force-displacement curves used to calibrate the non-linear spring on the simplified model are presented. In Figure 17, the deformed shapes of the model at points A (rollover, starting point of softening behavior) and point B (full contact, starting point of hardening behavior) are shown.

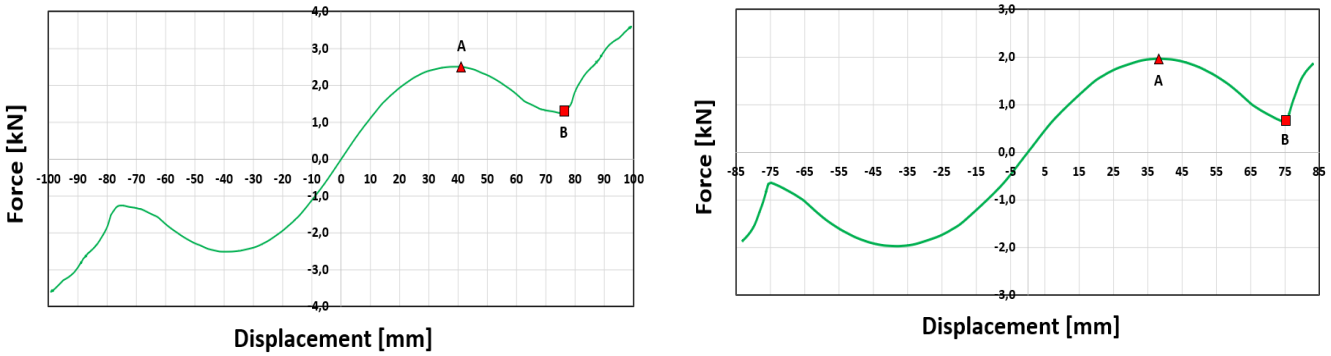

a) b)

Figure 16: Non-linear spring behavior obtained through direct shear analysis on the 3D model: cured at 150°C (a) and cured at 130°C (b), with instantaneous material properties

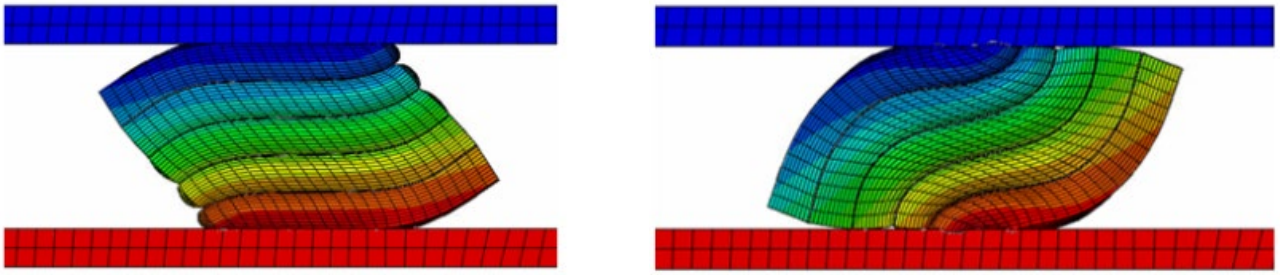

a) b)

Figure 17: Deformed shape of UFREI 75 at points A (a) and B (b) of Figure 16

Regarding the damping coefficient, it has been computed according to the procedure described in the previous section. The values used are summarized in Table 6.

Table 6: Damping coefficient used on the simplified spring-damper model

Model	Damping coefficient simplified model $[\frac{\mathbf{N\,s}}{\mathbf{mm}}]$
3D isolator cured at 150°	7.253
3D isolator cured at 130°	4.516

To assess the simplified model, cyclic shear analysis up to a lateral displacement of 50 mm analogous to the one described in the previous section has been performed. In Figure 18, a schematic representation of the model is presented. The results of the cyclic shear analysis on the simplified model have been compared with the 3D model ones. In Figure 19, the hysteresis force-displacement curves at each cycle related to the device cured at 150°C and at 130°C are presented.

As clearly visible, the simplified model is able to predict the stiffness of the 3D isolator in both cases. Conversely, a higher damping ratio is registered, especially at large displacement. However, the difference with the 3D model is acceptable from an engineering point of view thus the model could be usefully used at structural level.

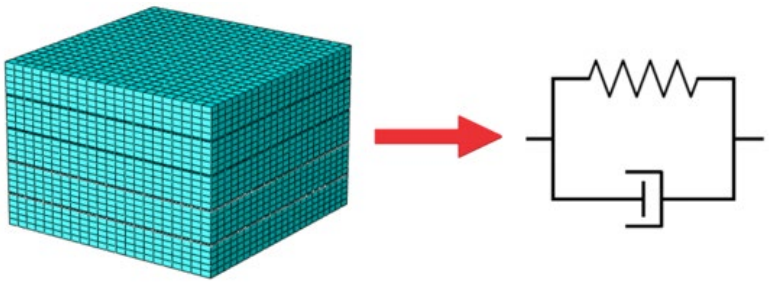

Figure 18: Simplified spring-damper model for cyclic shear analysis

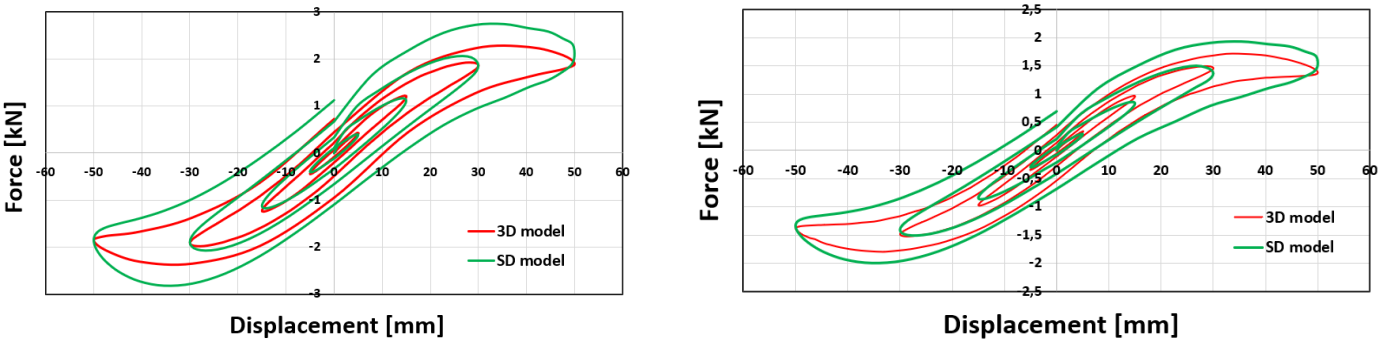

a) b)

Figure 19: Comparison between spring-damper model and 3D model at each cycle for the device cured at 150°C (a) and at 130°C (b)

5. Structural applications on isolated masonry

The UFREI devices under study are used to isolate a one storey masonry residential building. The numerical model involves a simplified model of UFREI, as discussed in the previous section. However, before the analysis on the isolated masonry, the accuracy of the simplified model is firstly evaluated through dynamic analysis on an isolated rigid slab, using four 3D detailed models of UFREIs at the corners. This analysis is useful to qualitatively understand UFREI 3D model behavior and it is used as a reference to validate the simplified spring-damper model discussed in the previous section. Once the simplified model is validated, it has been used to isolate a typical masonry structure. The dynamic performance has been assessed by evaluating displacement and acceleration time-history of a control point.

5.1. Rigid slab with FREI 3D model

Dynamic time-history analysis of an isolated rigid square slab has been performed using 3D detailed model of UFREIs. In Figure 20, a schematic representation of the model is shown. An unbonded condition has been used. A friction coefficient equal to μ=1 has been introduced between the supports and the isolators. For the accelerogram, a part of a real registration of L'Aquila earthquake (PGA=0,52 g) has been used, see Figure 21.

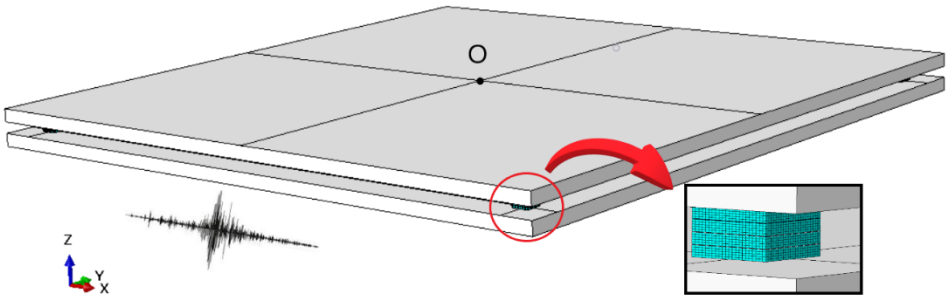

Figure 20: Model of the isolated rigid slab supported by 4 isolators subjected to a seismic excitation applied on x direction

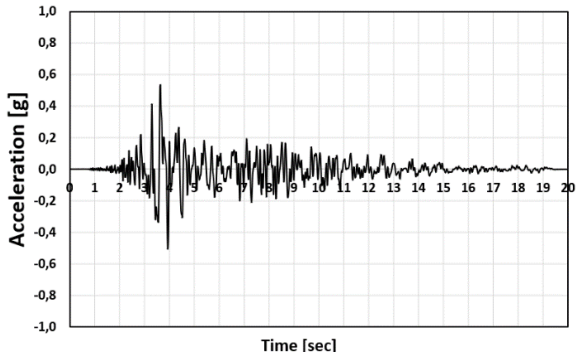

Figure 21: L'Aquila earthquake accelerogram (PGA=0,52g) used in the analysis

Time history acceleration of upper slab middle point *O* has been monitored to understand the capability of the UFREIs to reduce seismic excitation. In Figure 22, a comparison between time history point *O* accelerations obtained with under vulcanized device and with the well-vulcanized device is shown. The results are superimposed on the base slab acceleration.

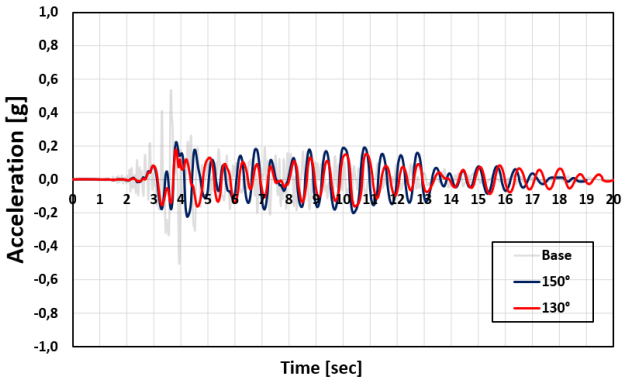

Figure 22: Comparison between point O acceleration obtained using FREI cured at 130°C and FREI cured at 150°C

As clearly visible, both the devices exhibit a good capability in reducing ground accelerations, and no important differences have been observed between the devices. Being the EPDM characterized by a small damping value, small oscillations at the end of the excitation have been registered in both cases.

According to the results obtained in the previous section, the under vulcanized device is characterized by smaller values of effective stiffness with respect to well-vulcanized device. Thus, deformed shapes of isolators at the PGA at t=3,8 s have been observed. As evident from Figure 23, largest deformation (up to almost 150% shear deformation) has been noticed on the under vulcanized device which experiences the full contact between its vertical edges and slab surface.

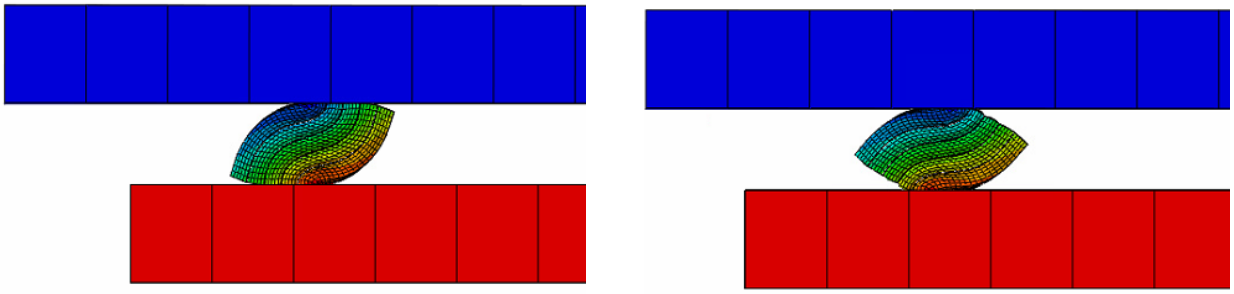

a) b)

Figure 23: deformed shape on the peak of under vulcanized device (a) and of the well-vulcanized device (b)

5.2. Rigid slab with the simplified model

As already pointed out, a spring-damper model has been built up to reduce the computational effort of the numerical analysis. Dynamic time-history analysis on the simplified model has been performed to understand whether it can catch the 3D isolator behavior qualitatively.

In Figure 24, the point *O* acceleration time-history of 3D models are compared with the simplified ones. As shown, being a single degree of freedom instrument, the simplified model is incapable of predicting the complex 3D behavior of the isolator perfectly. However, it can catch the behavior on the peak. Thus, it can be used as a valid tool for structural analysis purposes.

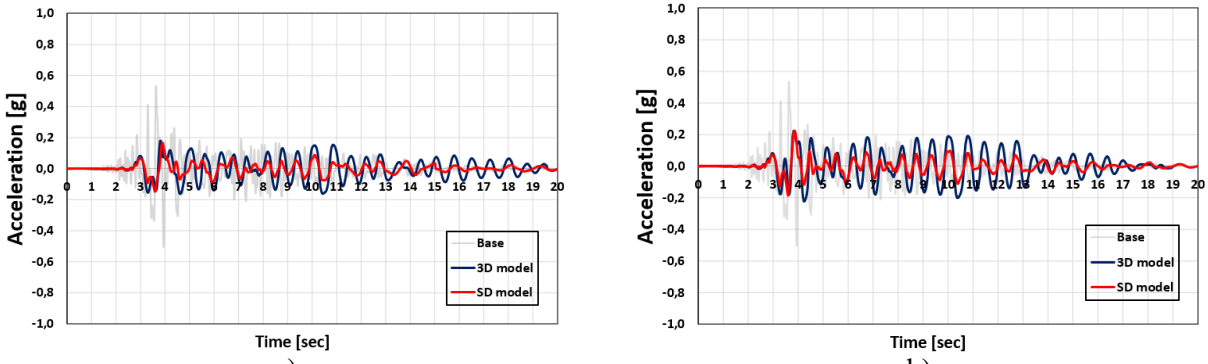

a) b)

Figure 24: Comparison between point O acceleration obtained with the 3D model and with the spring-damper simplified model for the under vulcanized device (a) and for the well vulcanized one (b)

5.3. Non-linear time history analysis on isolated one storey masonry housing

After validating the simplified spring-damper model, non-linear time history (NLTH) analyses have been performed on one storey masonry housing, isolated using the spring-damper simplified model. A

total of 16 UFREI75 has been installed.

Firstly, to evaluate the effectiveness of the isolation system, modal analysis has been executed. Subsequentially, non-linear dynamic analysis has been performed. The seismic performance is then assessed by evaluating the displacement time-history of a control point, the roof accelerogram and the tension damage map cumulated at the end of the numerical simulation.

The one storey masonry house presents a square area of 4m x 4m (LxL) and a height of 3m (H). The wall thickness is equal to 150 mm (Figure 25a). A timber roof has been added to the structure and some rigid beams on top of the windows and on the doors have been added to prevent premature flexural damage of the walls. The total weight of the prototype is approximately 18 tons.

For the numerical modeling, all the parts have been constrained with the surface-to-surface tie constraint available in Abaqus. The model has been discretized using approximately 3000 eight-node hexahedral linear elements with reduced integration (C3D8R), as shown in Figure 25b.

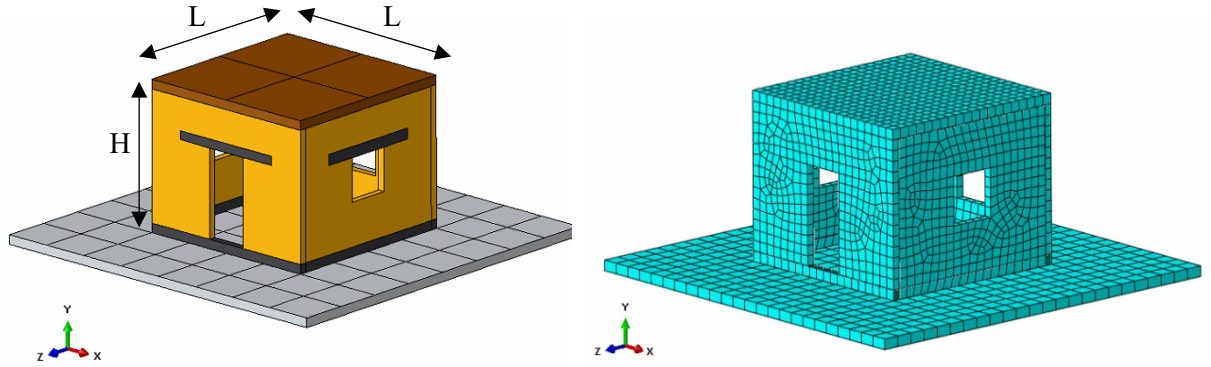

Sa) b)

Figure 25: 3D FE model (a) and 3D mash (b) of the low-rise masonry house prototype

Table 7: Mechanical elastic properties for masonry and timber

Material	**Density ρ [kg/m^3]**	**Young's modulus E [MPa]**	**Poisson's ratio υ [-]**
Timber	1000	7000	0
Masonry	1900	690	0.15

Timber has been considered as linear isotropic. The elastic mechanical properties of masonry and timber have been summarized in Table 7. The masonry material has been considered as isotropic material exhibiting damage both in tension and compression. Although this is a simplification, it is generally accepted in engineering practice. Table C8A.2.1 of the Explicative Notes of the Italia Building Code [39] has been adopted to choose its mechanical properties. The parameters in Table 8 are representative of poor-quality masonry consisting of irregular stones, which has been considered

suitable for low-rise buildings of developing countries.

To perform dynamic analysis, post-elastic constitutive law has been defined for masonry. Concrete damage plasticity (CDP) model has been used as a plasticity based damage model. Even if this model is generally employed for quasi-brittle materials such as concrete, it could be used for modeling other materials with distinct behavior in tension and compression, such as masonry [40][41].

In Table 8, the parameters adopted for the CDP model [42] are summarized, while in Table 9 and Figure 26, the elastic softening behaviors in compression and tension adopted for masonry are shown.

Table 8: Concrete Damage Plasticity parameters

Dilatancy angle [°]	Eccentricity [-]	f_{bo}/f_{co} [-]	K_c [-]	Viscosity parameter [-]
10°	0.1	1.16	0.667	0.002

Table 9: Stress-strain values considered in the CDP model for masonry

Masonry – Concrete Damage Plasticity			
Compression		**Tension**	
$\xi_{plastic}$ [-]	σ [MPa]	$\xi_{plastic}$ [-]	σ [MPa]
0	1.22	0	0.04
0.005	0.95	0.003	0.0005
0.01	0.95	0.1	0.0005
0.1	0.8	**Damage in tension**	
		$\xi_{plastic}$ [-]	DAMAGET
		0	0
		0.003	0.925

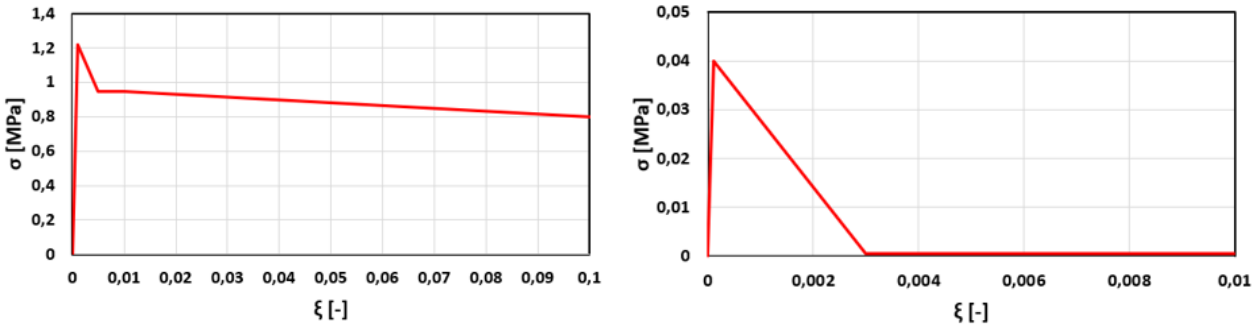

a) b)

Figure 26: Stress strain in compression (a) and tension (b) adopted for masonry in the CDP

Modal analysis has been performed to evaluate the natural periods of the structure with and without base isolation. As shown in Table 10, the implementation of isolators significantly shifts the natural periods to large values. In particular, the period is increased almost four times compared to the one without isolation. Moreover, the natural vibration modes pass from local to global. Figure 27, Figure

28 and Figure 29 show comparisons between vibration modes of isolated and fixed base structures.

Table 10: Natural periods of the masonry house with and without isolation

Mode	Fixed base	Isolated with device cured at 130°C	Isolated with device cured at 150°C
1	0.148	0.66	0.60
2	0.138	0.64	0.57
3	0.128	0.60	0.53

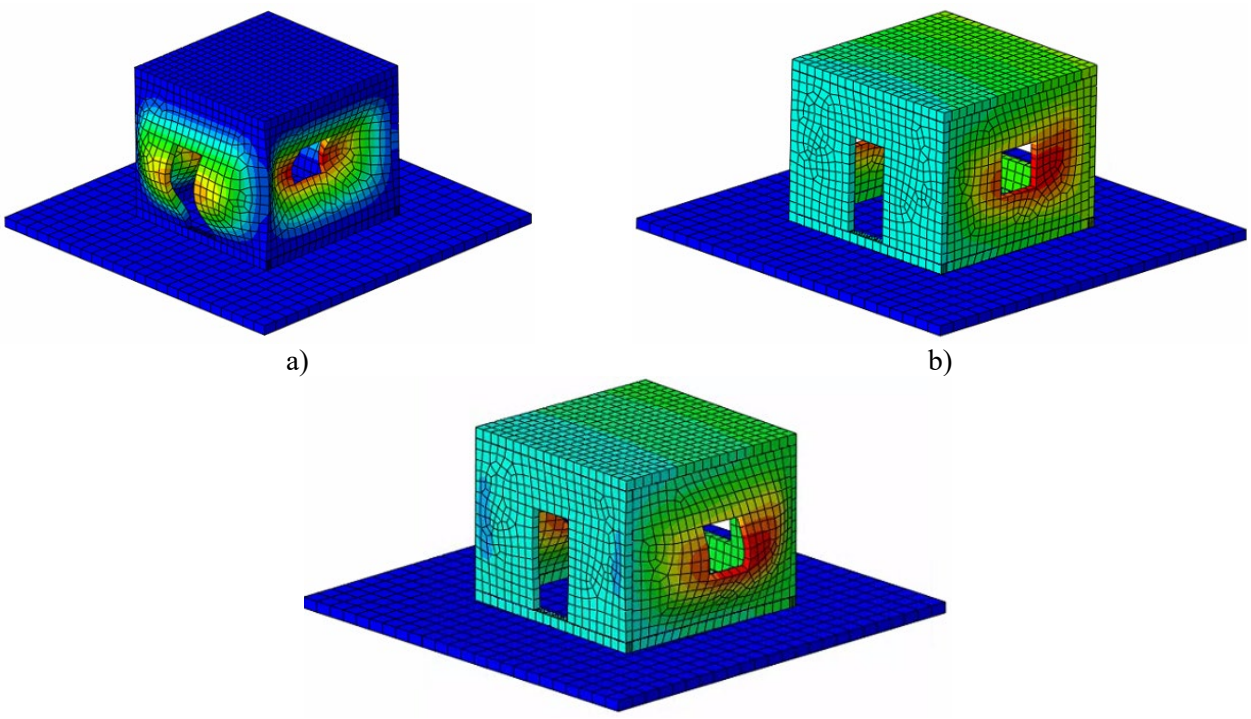

a) b)

c)

Figure 27: Mode 1 - fixed base (a), isolated with devices cured at 130° (b), isolated with devices cured at 150° (c)

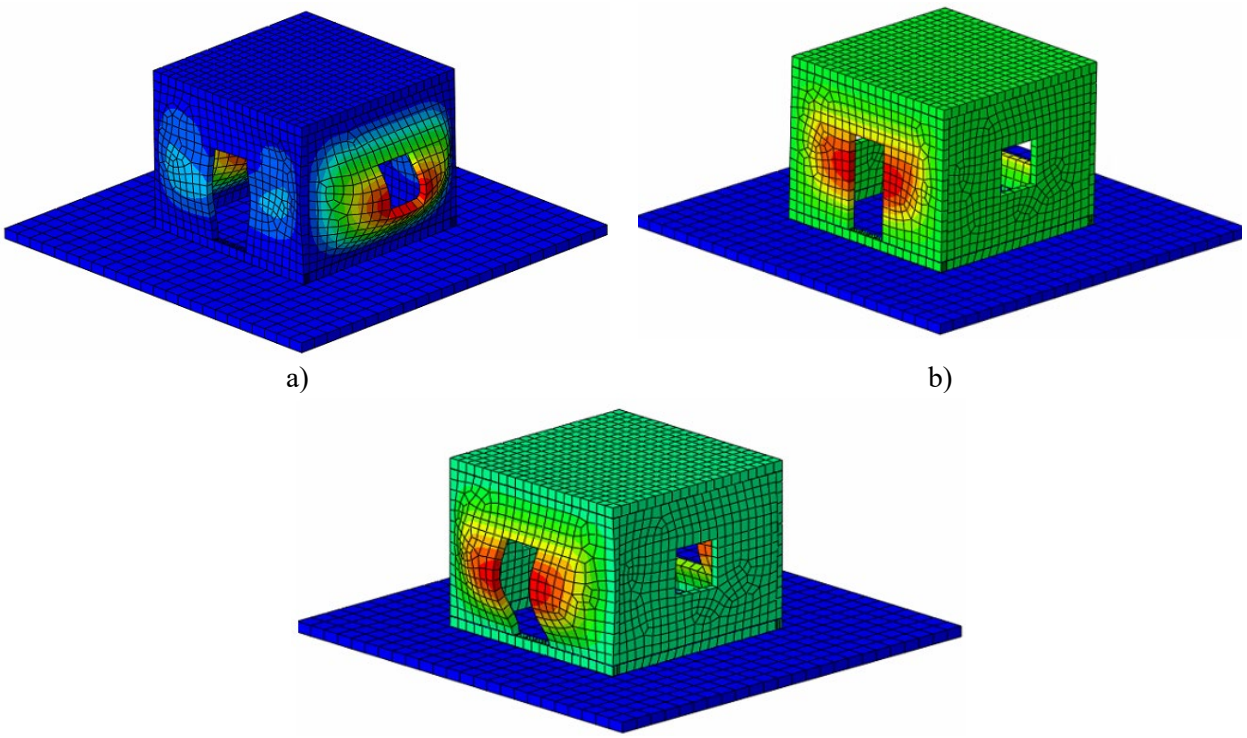

a) b)

c)

Figure 28: Mode 2 - fixed base (a), isolated with devices cured at 130° (b), isolated with devices cured at 150° (c)

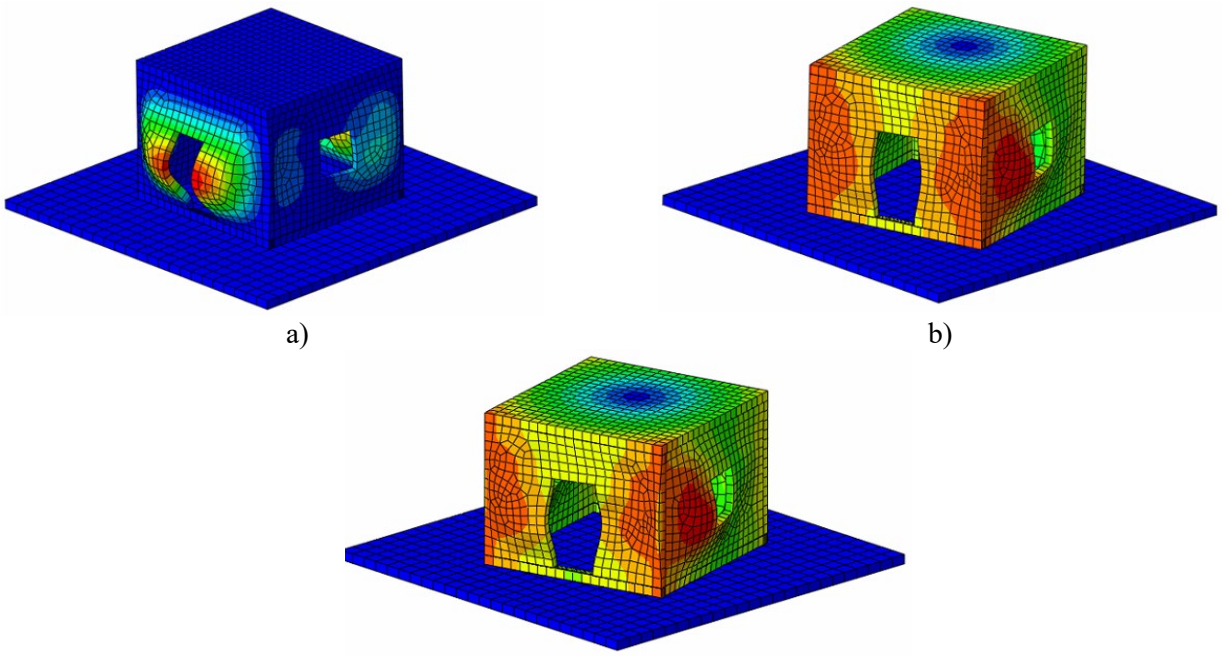

a) b)

c)

Figure 29: Mode 3 - fixed base (a), isolated with devices cured at 130° (b), isolated with devices cured at 150° (c)

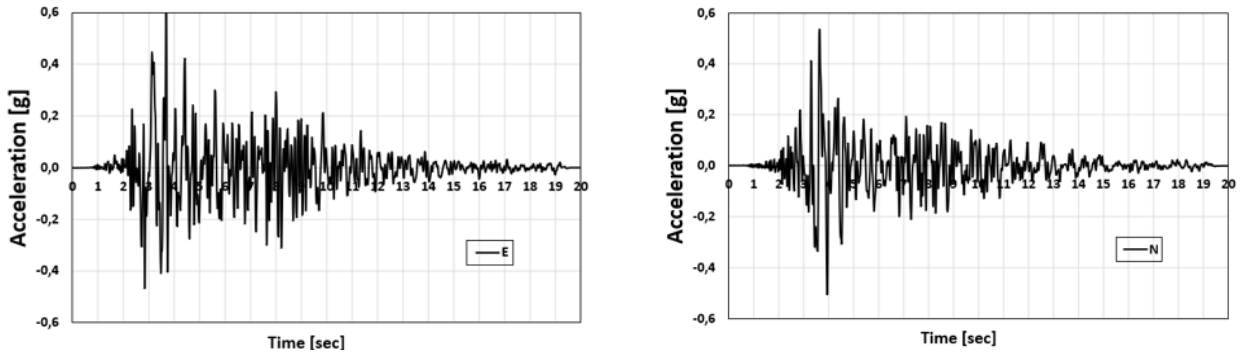

a) b)

Figure 30: East (a) and North (b) accelerogram component of 2009 L'Aquila earthquake

To evaluate the performance of the UFREIs, an NLTH analysis has been performed. Two accelerograms in both X and Z directions have been applied on the rigid base plate. The accelerograms are part of real registrations of N-E 2009 L'Aquila earthquake with a PGA of 0.62g (Figure 30). The seismic performance is investigated through displacement time-history of a control point on the roof (the prototype is characterized by box behavior due to the roof), top acceleration and map of cumulated damage in tension.

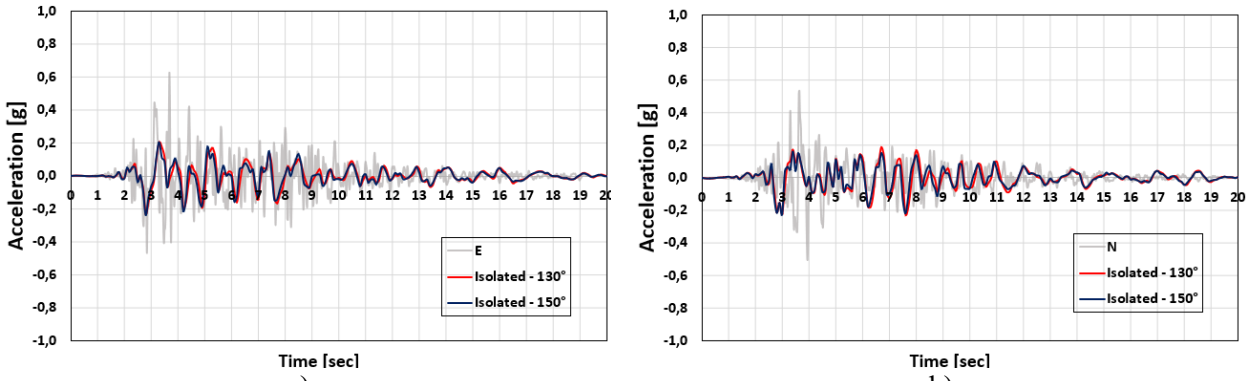

a) b)

Figure 31: Comparison between X direction (a) and Z direction (b) roof acceleration for both the model

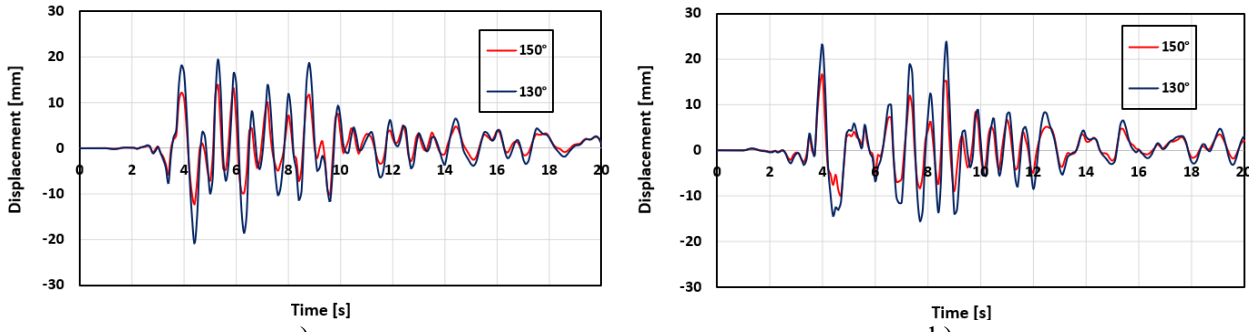

a) b)

Figure 32: Comparison between roof point displacement time history on x direction for both the model

In Figure 31, a comparison between roof acceleration in X and Z directions for both the model is represented. As visible, both the devices can reduce base acceleration and no remarkable differences have been noticed. In line with what happened in the slab, small oscillations of the house prototype at

the end of the seismic excitation have been recorded.

In Figure 32, a comparison between displacement time-history of roof control point is shown. Even in this case, the results are in line with what was noticed on the slab. Being the device cured at 130° less stiff with respect to the one cured at 150°, the house prototype isolated with the first experiences higher displacements.

Finally, the degradation of masonry has been described through a damage map after the seismic excitation, as seen in Figure 33. It is worth noting that the value of the DAMAGET varies from 0 (undamaged material - Blue) to 1 (no remaining stiffness - Red).

It can be seen that both isolators can significantly reduce the tensile damage on the structure. Moreover, being the isolators cured at 130° less stiff, the seismic demand is lower than the one in the prototype isolated with devices cured at 150°. For this reason, the tensile damage on the first case is slightly lower.

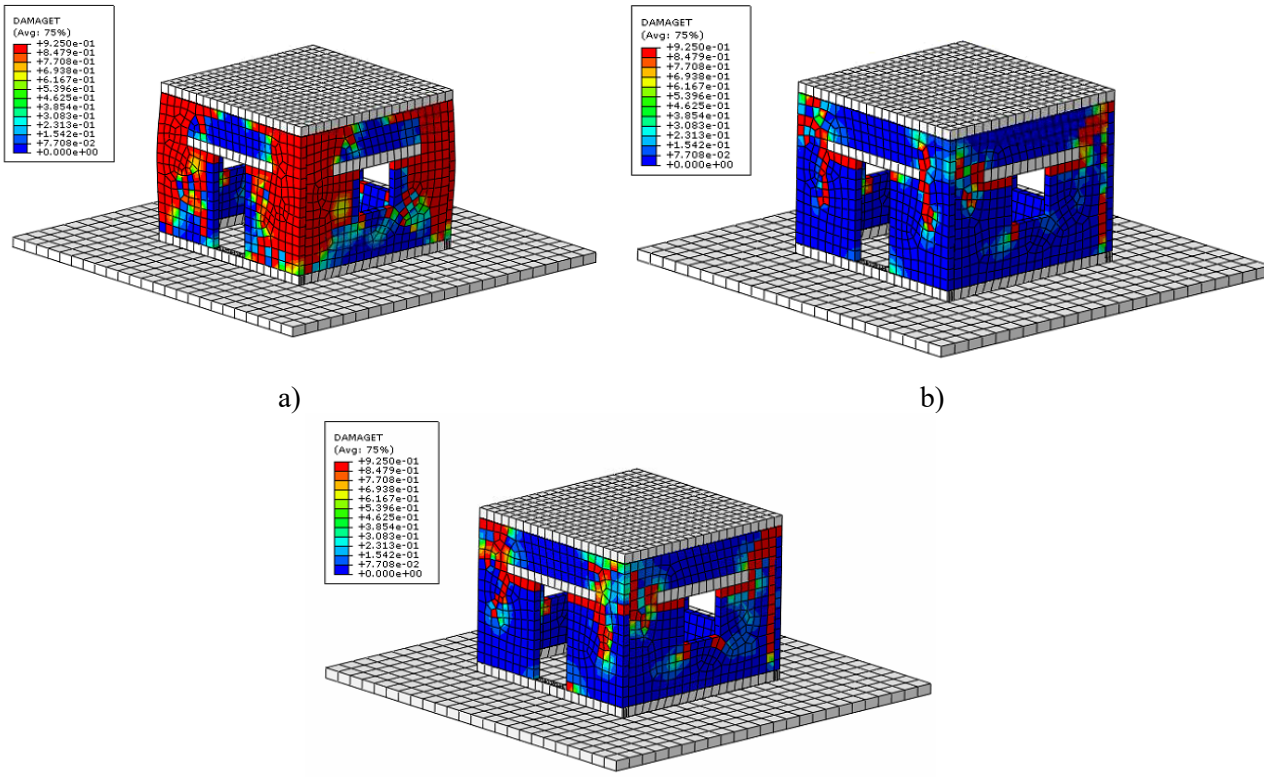

Figure 33: Tensile damage distribution for a masonry house prototype subjected to 0.6g L'Aquila earthquake: fixed base (a), isolated with devices cured at 130°C (b) and isolated with devices cured at 150°C (c)

6. Conclusions

In this paper, the seismic performance of under-vulcanized UFREI75 has been studied and compared with a well-vulcanized one.

After a double knife-cut on the device, Shore A hardness has been measured on the middle vertical section and along device diagonal. It was found that the hardness varies from inner to outer points passing from 48±2 Shore A to 60±2 Shore A, confirming that the mechanical properties are not homogenously distributed within the under vulcanized isolator.

Uniaxial tensile tests and relaxation tests were performed to obtain the hyperelastic and viscoelastic properties of the rubber pads in case of Shore A equal to 50 (S soft rubber) and 53 (H hard rubber). Such experimentation was crucial to correctly define a 3D FE model that has been used to simulate the cyclic shear behavior of the real under vulcanized isolator. The experimental values have been inserted on Abaqus to be fitted with the Yeoh model (Hyperelasticity) and the Prony model (Viscoelasticity).

Cyclic shear analyses have been performed and equivalent damping ratio and effective stiffness have been measured. Both models experience the typical rollover due to unbonded conditions and both damping and stiffness decrease with large displacement. By comparing the Lateral Force–Displacement curves it is evident how the under vulcanized device is less rigid with respect to the well vulcanized one.

A simplified spring-damper model has been introduced to use it in structural application. This was necessary due to the high computational cost of the isolator 3D model. To calibrate the non-linear spring, shear analysis has been performed on Abaqus using only instantaneous mechanical properties. Regarding the damping, a constant damping coefficient evaluated during cyclic shear analysis on the 3D model has been adopted. To assess the simplified model, cyclic shear analysis has been repeated on the simplified model. The results confirm that the spring-damper model can be a useful tool to replace the 3D model.

Two structural applications have been shown. In the first example, four 3D model isolators have been introduced between two rigid slabs. The base slab has been subjected to a seismic excitation using a part of a real accelerogram of L'Aquila earthquake (0.6 PGA). Top slab acceleration has been used as a reference to evaluate the seismic performance. Both the devices can reduce the base acceleration. However, by comparing the deformed shape on the PGA, it is evident how the under vulcanized device, being less rigid, experiences larger deformation with respect to the well-cured device, undergoing to full contact between its vertical edge and supports. Moreover, in both models, being the EPDM characterized by low damping capability, small oscillations have been recorded at the end of the seismic excitation.

In the second example, a fully non-linear dynamic analysis has been performed on a low-rise masonry house prototype using the simplified spring damping model. To understand the dynamic performance, three outputs have been chosen: top acceleration, top displacement time-history and tensile damage on masonry. According to the results, it can be stated that both the isolators can reduce damages on the structure. Moreover, being the under vulcanized device less rigid, it reduces more the seismic demand on the structure, thus low values of tensile damage have been noticed. In line with what found in the first example, by superimposing top acceleration and displacement time-history, it is evident how both the devices can reduce base acceleration, with higher values of displacement recorded for the under vulcanized device.

7. References

[1] G. Promis, E. Ferrier, P. Hamelin, "Effect of external FRP retrofitting on reinforced concrete short columns for seismic strengthening," Compos. Struct., 2009, doi: 10.1016/j.compstruct.2008.04.019.

[2] A. Ilki, O. Peker, E. Karamuk, C. Demir, N. Kumbasar, "FRP Retrofit of Low and Medium Strength Circular and Rectangular Reinforced Concrete Columns," J. Mater. Civ. Eng., 2008, doi: 10.1061/(asce)0899-1561(2008)20:2(169).

[3] A. Formisano, L. Lombardi, F. M. Mazzolani, "Perforated metal shear panels as bracing devices of seismic-resistant structures," J. Constr. Steel Res., 2016, doi: 10.1016/j.jcsr.2016.07.006.

[4] M. Badoux, J. O. Jirsa, "Steel Bracing of RC Frames for Seismic Retrofitting," J. Struct. Eng., 1990, doi: 10.1061/(asce)0733-9445(1990)116:1(55).

[5] M. Martinez-Rodrigo, M. L. Romero, "An optimum retrofit strategy for moment resisting frames with non-linear viscous dampers for seismic applications," Eng. Struct., 2003, doi: 10.1016/S0141-0296(03)00025-7.

[6] V. A. Matsagar, R. S. Jangid, "Base Isolation for Seismic Retrofitting of Structures," Pract. Period. Struct. Des. Constr., 2008, doi: 10.1061/(asce)1084-0680(2008)13:4(175).

[7] M. Mezzi, F. Comodini, L. Rossi, "A base isolation option for the full seismic protection of an existing masonry school building," 2011, doi: 10.4203/ccp.96.72.

[8] Mikayel G. Melkumyan, "Base Isolation Retrofitting Design for the Existing 9 Story Large Panel Apartment Building," Int. J. Trend Sci. Res. Dev., 2020.

[9] M. Spizzuoco, A. Calabrese, G. Serino, "Innovative low-cost recycled rubber-fiber reinforced isolator: Experimental tests and Finite Element Analyses," Eng. Struct., 2014, doi: 10.1016/j.engstruct.2014.07.001.

[10] A. Calabrese, M. Spizzuoco, G. Serino, G. Della Corte, G. Maddaloni, “Shaking table investigation of a novel, low-cost, base isolation technology using recycled rubber,” Struct. Control Heal. Monit., 2015, doi: 10.1002/stc.1663.

[11] B. Y. Moon, G. J. Kang, B. S. Kang, J. M. Kelly, “Design and manufacturing of fiber reinforced elastomeric isolator for seismic isolation,” 2002, doi: 10.1016/S0924-0136(02)00713-6.

[12] J. Kelly, “Analysis of Fiber-Reinforced Elastomeric Isolators,” J. Seismol. Earthq. Eng., 1999.

[13] H. Toopchi-Nezhad, M. J. Tait, R. G. Drysdale, “Lateral Response Evaluation of Fiber-Reinforced Neoprene Seismic Isolators Utilized in an Unbonded Application,” J. Struct. Eng., 2008, doi: 10.1061/(asce)0733-9445(2008)134:10(1627).

[14] N. C. Van Engelen, P. M. Osgooei, M. J. Tait, D. Konstantinidis, “Partially bonded fiber-reinforced elastomeric isolators (PB-FREIs),” Struct. Control Heal. Monit., 2015, doi: 10.1002/stc.1682.

[15] A. B. Habieb, G. Milani, T. Tavio, “Two-step advanced numerical approach for the design of low-cost unbonded fiber reinforced elastomeric seismic isolation systems in new masonry buildings,” Eng. Fail. Anal., vol. 90, no. March, pp. 380–396, 2018, doi: 10.1016/j.engfailanal.2018.04.002.

[16] N. C. Van Engelen, D. Konstantinidis, M. J. Tait, “Structural and nonstructural performance of a seismically isolated building using stable unbonded fiber-reinforced elastomeric isolators,” Earthq. Eng. Struct. Dyn., 2016, doi: 10.1002/eqe.2665.

[17] A. B. Habieb, M. Valente, G. Milani, “Base seismic isolation of a historical masonry church using fiber reinforced elastomeric isolators,” Soil Dyn. Earthq. Eng., vol. 120, no. January, pp. 127–145, 2019, doi: 10.1016/j.soildyn.2019.01.022.

[18] V. N. Thuyet, S. K. Deb, A. Dutta, “Mitigation of Seismic Vulnerability of Prototype Low-Rise Masonry Building Using U-FREIs,” J. Perform. Constr. Facil., 2018, doi: 10.1061/(asce)cf.1943-5509.0001136.

[19] M. G. P. De Raaf, M. J. Tait, H. Toopchi-Nezhad, “Stability of fiber-reinforced elastomeric bearings in an unbonded application,” J. Compos. Mater., 2011, doi: 10.1177/0021998310388319.

[20] V. Bernardo, T. Krejčí, T. Koudelka, M. Šejnoha, “Homogenization of unreinforced old masonry wallcomparison of scalar isotropic and orthotropicdamage models”, Acta Polytechnica CTU Proceedings 26:1–6, 2020, doi: 10.14311/APP.2020.26.0001.

[21] T. Krejčí, T. Koudelka, V. Bernardo, M. Šejnoha, “Effective elastic and fracture properties of regular and irregular masonry from nonlinear homogenization”, Computers & Structures,

Volume 254, 2021, doi: 10.1016/j.compstruc.2021.106580.

[22] F. Clementi, “Failure analysis of apennine masonry churches severely damaged during the 2016 central Italy seismic sequence”, Buildings 2021, 11, 58, doi: 10.3390/buildings11020058.

[23] F. Clementi, V. Gazzani, M. Poiani, S. Lenci, “Assessment of seismic behaviour of heritage masonry buildings using numerical modelling”, Journal of Building Engineering, Volume 8, 29-47. 2016, doi: 10.1016/j.jobe.2016.09.005.

[24] A. Pierdicca, F. Clementi, D. Isidori, E. Concettoni, C. Cristalli, S. Lenci, “Numerical model upgrading of a historical masonry palace monitored with a wireless sensor network”, International Journal of Masonry Research and InnovationVolume 1, Issue 1, Pages 74 – 98, 2016, doi: 10.1504/IJMRI.2016.074748.

[25] G. Pianese, G. Milani, R. Cerchiaro, M. Federico, “Optimal Vulcanization of Unbonded Fiber Reinforced Elastomeric Isolator Devices. Chemical Engineering Transactions”, 86, 1321-1326, 2020, doi: 10.3303/CET2186221.

[26] A. B. Habieb, F. Milani, G. Milani, R. Cerchiaro, “Rubber compounds made of reactivated EPDM for fiber-reinforced elastomeric isolators: an experimental study,” Iran. Polym. J. (English Ed.), vol. 29, no. 11, pp. 1031–1043, 2020, doi: 10.1007/s13726-020-00859-9.

[27] ISO 7619-1, “Rubber, vulcanized or thermoplastic - Determination of indentation hardness - Part 1: Durometer method (Shore hardness)”, 2010.

[28] ISO 37, “Rubber, vulcanized or thermoplastic - Determination of tensile stress-strain properties”, 2017.

[29] “Abaqus/Standard User’s Manual, Version 6.13.” .

[30] O. H. Yeoh, “Some forms of the strain energy function for rubber”, Rubber Chem. Technol., 1993, doi: 10.5254/1.3538343.

[31] P. Ghosh, A. Saha, P. C. Bohara, R. Mukhopadhyay, “Material property characterization for finite element analysis of tires”, Rubber World. 2006.

[32] T. Chen, “Determining Viscoelastic Strain Data a Prony Material Series for a From Time Varying”, Nasa, 2000.

[33] T. Dalrymple, J. Choi, K. Miller, “Elastomer rate-dependence: a testing and material modelling methodology”, Presented at the Fall 172nd Technical Meeting of the Rubber Division of the American Chemical Society, Inc, 2007.

[34] A. B. Habieb, M. Valente, G. Milani, “Hybrid seismic base isolation of a historical masonry church using unbonded fiber reinforced elastomeric isolators and shape memory alloy wires”, Eng. Struct., vol. 196, no. April, p. 109281, 2019, doi: 10.1016/j.engstruct.2019.109281.

[35] M. A. Kraus, M. Schuster, J. Kuntsche, G. Siebert, J. Schneider, “Parameter identification methods for visco- and hyperelastic material models”, Glas. Struct. Eng., 2017, doi: 10.1007/s40940-017-0042-9.

[36] P. M. Osgooei, M. J. Tait, D. Konstantinidis, “Finite element analysis of unbonded square fiber-reinforced elastomeric isolators (FREIs) under lateral loading in different directions”, Compos. Struct., vol. 113, no. 1, pp. 164–173, 2014, doi: 10.1016/j.compstruct.2014.02.033.

[37] T. Van Ngo, A. Dutta, S. K. Deb, “Evaluation of horizontal stiffness of fibre-reinforced elastomeric isolators”, Earthq. Eng. Struct. Dyn., 2017, doi: 10.1002/eqe.2879.

[38] N. C. Van Engelen, P. M. Osgooei, M. J. Tait, D. Konstantinidis, “Experimental and finite element study on the compression properties of Modified Rectangular Fiber-Reinforced Elastomeric Isolators (MR-FREIs)”, Eng. Struct., 2014, doi: 10.1016/j.engstruct.2014.04.046.

[39] Ministero delle Infrastrutture e dei Trasporti, “C.M. Infrastrutture e Trasporti 2 febbraio 2009, n° 617 - Istruzioni per l’applicazione delle ‘Norme Tecniche per le Costruzioni”, Gazz. Uff. della Repubb. Ital. 26 febbrario 2009, n° 47, Suppl. Ord. n° 27, 2009.

[40] M. Valente, G. Milani, “Non-linear dynamic and static analyses on eight historical masonry towers in the North-East of Italy”, Eng. Struct., 2016, doi: 10.1016/j.engstruct.2016.02.004.

[41] G. Castellazzi, A. M. D’Altri, S. de Miranda, F. Ubertini, “An innovative numerical modeling strategy for the structural analysis of historical monumental buildings”, Eng. Struct., 2017, doi: 10.1016/j.engstruct.2016.11.032.

[42] M. Acito, E. Magrinelli, G. Milani, S. Tiberti, “Seismic vulnerability of masonry buildings: Numerical insight on damage causes for residential buildings by the 2016 central Italy seismic sequence and evaluation of strengthening techniques”, J. Build. Eng., vol. 28, no. November 2019, p. 101081, 2020, doi: 10.1016/j.jobe.2019.101081.